Available online at www.sciencedirect.com
ScienceDirect
Journal of Computational Physics 227 (2008) 6206–6225
JOURNAL OF COMPUTATIONAL PHYSICS
www.elsevier.com/locate/jcp

Computationally fast harmonic balance methods for unsteady aerodynamic predictions of helicopter rotors ☆

Kivanc Ekici *, Kenneth C. Hall, Earl H. Dowell

Duke University, Department of Mechanical Engineering and Materials Science, 144 Hudson Hall, Box 90300, Durham, NC 27708-0300, USA

Received 5 July 2007; received in revised form 21 February 2008; accepted 26 February 2008
Available online 8 March 2008

Abstract

A harmonic balance technique for the analysis of unsteady flows about helicopter rotors in forward flight and hover is presented in this paper. The aerodynamics of forward flight are highly nonlinear, with transonic flow on the advancing blade, subsonic flow on the retreating blade, and stalled flow over the inner portion of the rotor. Nevertheless, the unsteady flow is essentially periodic in time making it well suited for frequency domain analysis. The present method uses periodic boundary conditions that allows one to model the flow field on a computational grid around a single helicopter blade, no matter the actual blade count. Using this approach, we compute several solutions, each one corresponding to one of several instants in time over one period. These time levels are coupled to each other through a spectral time derivative operator in the interior of the computational domain and through the far-field and periodic boundary conditions around the boundary of the domain. In this paper, we apply the method to the three-dimensional Euler equations (although the method can also be applied to three-dimensional viscous flows), and examine the steady and unsteady aerodynamics about wings and rotors.
© 2008 Elsevier Inc. All rights reserved.

Keywords: Computational fluid dynamics; Unsteady aerodynamics; Helicopter rotors; Harmonic balance technique; Frequency-domain methods

1. Introduction

Rotorcraft aerodynamics is one of the most challenging problems in computational fluid dynamics (CFD) because of the complex flow involved including unsteadiness and viscous phenomena. Helicopter rotor blades create unsteady vortical wakes that create a downwash which affects the angle of attack of the rotor. Tip vortices interact with the other blades of the rotor and may create significant noise and vibration. In forward flight, the flow is highly nonlinear with transonic flow on the advancing blade, and subsonic flow on the

☆ Presented at the 46th AIAA Aerospace Sciences Meeting and Exhibit (Reno, Nevada, January 2008).

* Corresponding author. Tel.: +1 919 660 5348; fax: +1 919 660 8963.
E-mail addresses: ekici@duke.edu (K. Ekici), kenneth.c.hall@duke.edu (K.C. Hall), dowell@ee.duke.edu (E.H. Dowell).

0021-9991/$ - see front matter © 2008 Elsevier Inc. All rights reserved.
doi:10.1016/j.jcp.2008.02.028

retreating blade, with stalled flow over the inner portion of the rotor for high speeds. Because of the aforementioned complexities, the application of computational helicopter rotor aerodynamics has lagged behind that in fixed-wing aircraft. Nevertheless, a number of researchers have contributed to the understanding of complex unsteady aerodynamics of rotorcraft using CFD. Earlier CFD analysis tools for rotorcraft aerodynamics have included transonic full potential models [1,2]. While these methods provide solutions at relatively low cost, they may not capture some of the flow features that are important in determining the aerodynamic performance of the rotor. Therefore, over the past couple of decades the Euler/Navier–Stokes analyses [3–14] have become prevalent. For a complete review of the challenges and the state of the art in rotorcraft aerodynamics, we refer the reader to the review papers of Conlisk [15] and Strawn et al. [16].

As computer power increases, increasingly sophisticated computer fluid dynamic models of unsteady flows about helicopter rotors are being developed. It is now conceivable to perform time-accurate large eddy simulations (LES) of unsteady flows about helicopter rotors, albeit with considerable computational effort. If successful, these techniques may provide more accurate solutions than currently available. However, such codes will be – without additional breakthroughs in computer or algorithm technology – extremely expensive to use, requiring significant computer resources. This will make them difficult to use in a design mode, where many thousands of flight conditions and/or designs might be analyzed. Furthermore, these advanced CFD techniques, while providing detailed information about the flow field, do not directly provide insight into how to design helicopters for improved aerodynamic and aeroacoustic performance. In the work presented in the literature to date, investigators have used time-accurate CFD methods, requiring significant amounts of computational power and time, to analyze the nonlinear forward-flight aerodynamics of helicopter rotors.

The fact that the unsteady flow about helicopter rotors is temporally and spatially periodic makes it well suited for frequency domain analysis. In the turbomachinery community, the need for efficient nonlinear unsteady flow solvers led investigators to develop efficient mixed time and frequency-domain techniques. Hall et al. [17–19] proposed the "harmonic balance" approach. In his original approach, Hall [17] represented periodic unsteady flows by a Fourier series in time with frequencies that are integer multiples of the original excitation frequency. The dependent variables were the Fourier coefficients of the Fourier series for each of the conservation variables. These Fourier series were then inserted into the Euler or Navier–Stokes equations, and the resulting expressions were "balanced", that is, the resulting expressions were expanded, and terms were collected frequency by frequency. For the Euler or Navier–Stokes equations to be satisfied, each frequency component must vanish independently. The result is a set of coupled complex partial differential equations, one for each frequency retained in the model. Time derivatives in the nth equation were replaced by $j\omega n$. Because time does not appear explicitly, the harmonic balance equations can be solved very efficiently using the same numerical algorithms developed for steady-state flow problems.

The computational cost of the original form of the harmonic balance equations did not scale well with the number of harmonics included in the model. Furthermore, the algebraic balancing does not work well with more complicated equations such as the Navier–Stokes equations with turbulence models. To eliminate these problems, Hall et al. [18,19] developed an improved version of the harmonic balance technique in which the dependent variables are the conservation variables stored at a number of sub-time levels over one period. This approach is somewhat similar to the dual time step approach [20], except that in the harmonic balance method several time levels are stored, and one makes use of the temporal periodicity of the flow. In the dual time step approach, one marches the solution from one physical time level to the next. Within each of these time steps, a number of pseudo-time steps are taken to improve the accuracy of the physical time stepping solution. In the harmonic balance technique, on the other hand, all physical time levels are computed simultaneously, with pseudo-time marching used to drive the solution to convergence. The various physical time levels are only coupled to one another through the periodic boundary conditions (blade to blade periodicity), and through a pseudo-spectral operator that approximates the time derivatives in the Euler or Navier–Stokes equations. The advantage of this modified harmonic balance approach is that the computational cost scales (nearly) linearly with the number of time levels retained in the model. Furthermore, use of the pseudo-spectral time derivative operator allows one to use a small number of time levels (or equivalently harmonics) to obtain quite accurate solutions. The resulting equations are mathematically equivalent to steady equations and, therefore, convergence acceleration techniques used to speed convergence of steady flow solvers may be applied. The main disadvantage of the harmonic balance approach is the increased memory requirement due to the storage

of the different time level solutions. This may be a problem if a large number of sub-time levels must be retained in the analysis. In such cases, parallel computing may be used to avoid the memory requirement problems.

A number of investigators have contributed to the development of the harmonic balance technique, or have used the technique to solve interesting fluid dynamic problems. Such problems include the vortex shedding of a circular cylinder [21,22], multistage turbomachinery analysis [23,24], limit-cycle oscillations of wings [25], and normal synthetic jet in quiescent background flow [26]. Recently, investigators [27,28] have started using similar techniques to analyze unsteady aerodynamics of helicopter rotors, and have demonstrated that accurate solutions can be obtained efficiently. In this work, we apply the state-of-the-art high-dimensional harmonic balance (HDHB) technique to helicopter rotors in forward-flight and demonstrate that large scale nonlinearities can be accurately modeled with substantially less computational effort than conventional time-accurate solution methods. A further advantage of the current approach is that since the harmonic balance equations are mathematically steady state equations, the resulting code would be well suited for an adjoint sensitivity analysis, leading ultimately to the ability to optimize rotors for performance and noise in a systematic way.

2. Harmonic balance theory

To motivate the HDHB approach, consider the three-dimensional Euler equations, given by

$$\frac{\partial \mathbf{U}}{\partial t}+\frac{\partial \mathbf{F}}{\partial x}+\frac{\partial \mathbf{G}}{\partial y}+\frac{\partial \mathbf{H}}{\partial z}+\mathbf{S}=0, \tag{1}$$

where x and y are coordinates in the plane of the helicopter rotor and z is the axis about which the rotor turns. The coordinate system is assumed here to rotate with the rotor at angular velocity Ω. The vector $\mathbf{U}$ is the vector of conservation variables, the vectors $\mathbf{F}$, $\mathbf{G}$, and $\mathbf{H}$ are so-called flux vectors, and $\mathbf{S}$ is a source term. For example, some of these vectors are given by

$$\mathbf{U}=\begin{bmatrix}\rho\\ \rho u\\ \rho v\\ \rho w\\ \rho e\end{bmatrix},\quad \mathbf{F}=\begin{bmatrix}\rho u\\ \rho u^2+p\\ \rho uv\\ \rho uw\\ \rho uI\end{bmatrix},\quad \mathbf{S}=\begin{bmatrix}0\\ -\rho(\Omega^2 y+2\Omega v)\\ -\rho(\Omega^2 x-2\Omega u)\\ 0\\ 0\end{bmatrix}. \tag{2}$$

Eqs. (1) and (2) represent the conservation of mass, three components of momentum, and energy, respectively. In the above equations, ρ is the density, u, v, and w are the velocity components in the x, y, and z and directions, respectively, e is the total internal energy, I is the total rothalpy, and p is the static pressure. For an ideal gas with constant specific heats, the rothalpy and pressure may be expressed in terms of the conservation variables, i.e.,

$$I=\frac{\rho e+p}{\rho}, \tag{3}$$

$$p=(\gamma-1)\rho\left[e-\frac{1}{2}(u^2+v^2+w^2)+\frac{1}{2}\Omega^2 r^2\right], \tag{4}$$

where r is the distance from the z axis ($r=\sqrt{x^2+y^2}$).

2.1. Classical harmonic balance method

For many flows of interest in helicopter aerodynamics, the flow (when viewed in the rotating frame of reference) is periodic in time, with period $T=2\pi/\Omega$. Because the flow is temporally periodic, the flow variables may be represented as a Fourier series in time with spatially varying coefficients. For example, the conservation variables may be expressed as

$$\rho(x,y,z,t) = \sum_n R_n(x,y,z)\mathrm{e}^{j\omega nt}, \quad \rho u(x,y,z,t) = \sum_n U_n(x,y,z)\mathrm{e}^{j\omega nt},$$
$$\rho v(x,y,z,t) = \sum_n V_n(x,y,z)\mathrm{e}^{j\omega nt}, \quad \rho w(x,y,z,t) = \sum_n W_n(x,y,z)\mathrm{e}^{j\omega nt}$$
$$\rho e(x,y,z,t) = \sum_n E_n(x,y,z)\mathrm{e}^{j\omega nt}, \tag{5}$$

where ω is the fundamental frequency Ω. In principle, the summations in these series are taken over all integer values of n. In practice, however, the series may be truncated to a finite number of terms, $-N \leqslant n \leqslant +N$.

Next, we substitute the series expansions for ρ, ρu, ρv, ρw, and ρe into the Euler equations. Conceptually, we can now expand the resulting expressions into Fourier series in time, grouping the resulting terms by frequency, and require each frequency component to sum to zero individually. Collecting the resulting equations together, including the equivalent mass and energy equations, into one vector equation gives

$$\tilde{\mathbf{Q}}(\tilde{\mathbf{U}}) + \frac{\partial \tilde{\mathbf{F}}(\tilde{\mathbf{U}})}{\partial x} + \frac{\partial \tilde{\mathbf{G}}(\tilde{\mathbf{U}})}{\partial y} + \frac{\partial \tilde{\mathbf{H}}(\tilde{\mathbf{U}})}{\partial z} + \tilde{\mathbf{S}}(\tilde{\mathbf{U}}) = 0, \tag{6}$$

where

$$\tilde{\mathbf{U}} = \begin{Bmatrix} R_0 \\ U_0 \\ V_0 \\ W_0 \\ E_0 \\ R_{+1} \\ U_{+1} \\ V_{+1} \\ W_{+1} \\ E_{+1} \\ \vdots \end{Bmatrix}, \quad \tilde{\mathbf{Q}} = j\omega \begin{Bmatrix} 0 \cdot R_0 \\ 0 \cdot U_0 \\ 0 \cdot V_0 \\ 0 \cdot W_0 \\ 0 \cdot E_0 \\ +1 \cdot R_{+1} \\ +1 \cdot U_{+1} \\ +1 \cdot V_{+1} \\ +1 \cdot W_{+1} \\ +1 \cdot E_{+1} \\ \vdots \end{Bmatrix} \tag{7}$$

The vectors $\tilde{\mathbf{F}}, \tilde{\mathbf{G}}$, and $\tilde{\mathbf{H}}$ contain the Fourier coefficients of the Fourier series expansion for the flux vectors. Similarly, $\tilde{\mathbf{S}}(\tilde{\mathbf{U}})$ contains the Fourier coefficients of the source term. $\tilde{\mathbf{Q}}(\tilde{\mathbf{U}})$ is the remnant of the time derivative term appearing in the original Euler equations. Finally, we note the conservation variables are real quantities, so that, for example,

$$U_{-n} = \overline{U}_n, \tag{8}$$

where $\overline{U}_n$ is the complex conjugate of U_n. Thus, we only need to store Fourier coefficients for non-negative n. If N harmonics are retained in the Fourier series representation of the flow, then $2N+1$ coefficients are stored for each flow variable (one for the zeroth harmonic or mean flow, and $2N$ for the real and imaginary parts of the remaining harmonics).

2.2. High-dimensional harmonic balance method

Computation of the harmonic fluxes in the classical harmonic balance approach is difficult and computationally expensive. The operation count is on the order of N^3, so that the cost of the harmonic balance analysis grows rapidly with the number of harmonics. To alleviate this difficulty, we note that alternatively one can store solutions at $2N+1$ equally spaced points in time over one period. In other words,

$$\mathbf{U}(x,y,z,t) \approx \mathbf{A}_0(x,y,z) + \sum_{n=1}^{N} [\mathbf{A}_n(x,y,z)\cos(\omega nt) + \mathbf{B}_n(x,y,z)\sin(\omega nt)], \tag{9}$$

where, $\mathbf{A}_0$, $\mathbf{A}_n$, and $\mathbf{B}_n$ are the Fourier coefficients of the flow variables. This expression can also be written in matrix form as

$$\mathbf{U}^* = \mathbf{E}^{-1}\tilde{\mathbf{U}}, \tag{10}$$

where $\mathbf{U}^*$ is the vector of conservation variables at $2N+1$ equally spaced points in time over one temporal period and $\mathbf{E}^{-1}$ is matrix that is the inverse discrete Fourier transform operator. As an example, assume that one retains five harmonics in the HDHB method so that

$$\underbrace{\begin{Bmatrix} \mathbf{U_1} \\ \mathbf{U_2} \\ \mathbf{U_3} \\ \vdots \\ \mathbf{U_{11}} \end{Bmatrix}}_{\mathbf{U}^*} = \underbrace{\begin{bmatrix} 1 & \cos\omega t_1 & \cdots & \cos\omega 5t_1 & \sin\omega t_1 & \cdots & \sin\omega 5t_1 \\ 1 & \cos\omega t_2 & \cdots & \cos\omega 5t_2 & \sin\omega t_2 & \cdots & \sin\omega 5t_2 \\ 1 & \cos\omega t_3 & \cdots & \cos\omega 5t_3 & \sin\omega t_3 & \cdots & \sin\omega 5t_3 \\ \vdots & & & & & & \\ 1 & \cos\omega t_{11} & \cdots & \cos\omega 5t_{11} & \sin\omega t_{11} & \cdots & \sin\omega 5t_{11} \end{bmatrix}}_{\mathbf{E}^{-1}} \underbrace{\begin{Bmatrix} \mathbf{A}_0 \\ \mathbf{A}_1 \\ \vdots \\ \mathbf{A}_5 \\ \mathbf{B}_1 \\ \vdots \\ \mathbf{B}_5 \end{Bmatrix}}_{\tilde{\mathbf{U}}} \tag{11}$$

Similarly, one can obtain the Fourier coefficients of the conservation variables using

$$\tilde{\mathbf{U}} = \mathbf{E}\mathbf{U}^*, \tag{12}$$

where $\mathbf{E}$ is the discrete Fourier transformation matrix. Next, we write the Euler equations at all sub-time levels simultaneously, so that

$$\frac{\partial \mathbf{U}^*}{\partial t} + \frac{\partial \mathbf{F}^*}{\partial x} + \frac{\partial \mathbf{G}^*}{\partial y} + \frac{\partial \mathbf{H}^*}{\partial z} + \mathbf{S}^* = 0, \tag{13}$$

where for example, $\mathbf{F}^*$ is the vector of x-fluxes evaluated at $\mathbf{U}^*$. Hence, Eq. (13) has $5 \times (2N+1)$ equations.

Note that the $2N+1$ sets of conservation equations in Eq. (13) are coupled only through the time derivative term, which is approximated by the pseudo-spectral operator, $\mathbf{D}$. To motivate the development of $\mathbf{D}$, we note that

$$\frac{\partial}{\partial t}\mathbf{U}^* = \sum_{n=1}^{N} [-\omega n \cdot \mathbf{A}_n \sin(\omega n t) + \omega n \cdot \mathbf{B}_n \cos(\omega n t)] \tag{14}$$

or in matrix form

$$\frac{\partial \mathbf{U}^*}{\partial t} = \frac{\partial \mathbf{E}^{-1}}{\partial t}\tilde{\mathbf{U}}. \tag{15}$$

Making use of Eq. (12) gives the desired pseudo-spectral operator

$$\frac{\partial \mathbf{U}^*}{\partial t} = \frac{\partial \mathbf{E}^{-1}}{\partial t}\mathbf{E}\mathbf{U}^* = \mathbf{D}\mathbf{U}^*. \tag{16}$$

Finally, substitution of Eq. (16) into Eq. (13) gives the desired harmonic balance equations, i.e.,

$$\mathbf{D}\mathbf{U}^* + \frac{\partial \mathbf{F}^*}{\partial x} + \frac{\partial \mathbf{G}^*}{\partial y} + \frac{\partial \mathbf{H}^*}{\partial z} = \mathbf{S}^*. \tag{17}$$

The advantage of Eq. (17) over the classical form of the harmonic balance equations, Eq. (6), is that the fluxes in Eq. (17) are much easier to compute (order N operations). The fluxes are simply computed at each of the $2N+1$ time levels in the usual way. Note that this form of the harmonic balance equations is similar to the nonlinear frequency domain (NLFD) form of McMullen et al. [22]. In the NLFD approach, the Fourier coefficients of the flow variables are solved and stored. When the computation of the residuals in the frequency domain is required, one first needs to transform the Fourier coefficients back to the time domain using an

inverse fast-Fourier transform (FFT). After that, the residuals are computed in the time domain and the Fourier coefficients of the residuals are computed using an FFT and the governing equations are solved in the frequency domain. The main advantage of the HDHB method is its ease of implementation to the existing steady-state codes. Similar to the NLFD approach, HDHB uses convergence acceleration techniques (multigrid acceleration and local time-stepping) and the convergence rate of the unsteady solution is equivalent to the convergence rate of the steady-state solution (see Section 5.3).

3. Numerical solution technique

To solve the harmonic balance equations, we introduce a "pseudo-time" term so that the equations may be marched rapidly to a steady-state condition using a conventional computational fluid dynamic scheme. Thus, Eq. (17) becomes

$$\frac{\partial \mathbf{U}^*}{\partial \tau} + \mathbf{D}\mathbf{U}^* + \frac{\partial \mathbf{F}^*}{\partial x} + \frac{\partial \mathbf{G}^*}{\partial y} + \frac{\partial \mathbf{H}^*}{\partial z} + \mathbf{S}^* = 0, \tag{18}$$

where τ is a fictitious or pseudo time, used only to march Eq. (18) to steady state, thereby driving the pseudo-time term to zero. Note that pseudo-time harmonic balance equations are similar in form to the original time-domain form of the Euler equations, Eq. (1). Thus, existing well-developed *steady* CFD techniques may be used to efficiently solve the nonlinear harmonic balance equations, with a similar number of iterations required. Eq. (18) is discretized on a computational grid spanning only a single blade sector. A typical grid is shown in Fig. 1. We use Ni's [29] two-step Lax–Wendroff scheme to discretize the harmonic balance equations. The Lax–Wendroff scheme is a node-centered conservative finite volume scheme. A combination of second and fourth difference smoothing is used to capture shocks. Also, because only "steady-state" solutions are desired, we use local time stepping and multiple-grid acceleration techniques to speed-up convergence.

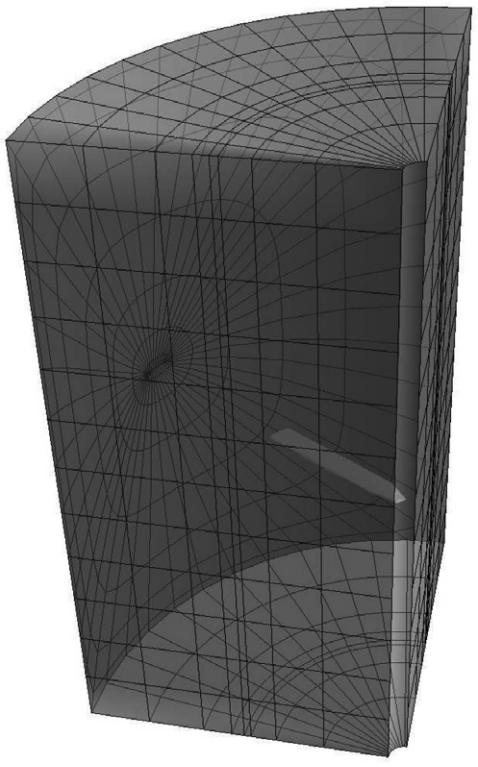

Fig. 1. Representative computational grid for a rotor sector.

In Eq. (18), we use a spectral operator to compute the time derivative term $\mathbf{DU}^*$. As presented, this operator requires $\mathcal{O}(N^2)$ operations to compute; using fast Fourier transform techniques, the cost can be reduced to $\mathcal{O}(N\log(N))$. However, the calculation of the flux vector terms is greatly simplified, requiring only $\mathcal{O}(N)$ computations. For a small number of sub-time level solutions retained in the analysis ($N \leqslant 11$), the flux calculations require substantially more computational time than the relatively simple time derivative term. Thus, the computational time scales approximately like the number of Fourier terms retained in the solution, or, equivalently the number of time slices in $\mathbf{U}^*$. However, when the number of sub-time levels is large the cost of computing the time derivative increases.

The high-dimensional harmonic balance method as described here has some similarities to the "dual time step" method, used by Davis et al. [20], Sayma et al. [30], and others to compute unsteady flows in the time domain. Our approach, however, has a number of important advantages. First, in the dual time step method, one marches from one time level to the next time accurately, using pseudo-time to drive the residual of the time-accurate equations to zero. The process is repeated over many times steps for several periods T until a periodic solution has been reached. In our approach, we store the solution at just a few points over a single period, and the solutions at all these temporal points are advanced simultaneously using pseudo-time marching until the solution converges. Second, because we solve for the solution over one complete period, a spectral operator may be used to compute the physical time derivative $\partial/\partial t$. The spectral time derivative is much more accurate than finite difference operators, which are used in the dual time step approach. Therefore, many fewer physical time levels are required using the present method. Finally, previous work by the authors indicates that the resulting scheme may be much less dissipative than conventional time domain techniques, and thus better suited for computing aeroacoustic quantities.

The HDHB technique is applicable in all helicopter flight regimes, but will be especially efficient for any problem where the time-average or the low frequency content is important, for example the time-averaged aerodynamic performance, per rev vibrations and many acoustic problems including high speed impulsive noise. For these problems, it should be possible to estimate accurately the first two tones using on the order of nine to eleven time slices (four to five harmonics), a result that was also confirmed by Choi et al. [27]. Thus, the computational cost will approximately be ten times a single steady-flow computation.

4. Boundary conditions

The boundary conditions consist of surface, far-field, and periodic boundary conditions and are applied once at every iteration in the flow solver. On the blade surface, the flow tangency condition is imposed for the Euler equations.

At the far-field boundary, we apply one-dimensional Riemann boundary conditions as described in Thomas and Salas [31]. To summarize, at the grid nodes where the flow velocity is locally incoming, we prescribe four characteristics associated with the physical free-stream values; we compute the fifth characteristic from the internal values. In case of locally outgoing flow, on the other hand, one needs to specify only one characteristic associated with the specified free-stream; the remaining four characteristics are computed from the internal values.

In addition to temporal periodicity, the flow about a helicopter rotor also satisfies a certain spatial periodicity. That is, the flow about one blade is the same as the flow about a neighboring blade, but with a time shift. Consider a four-bladed rotor in forward-flight depicted in Fig. 2. The periodic boundary condition requires that the current solution at point a is the same as the solution at point b at an earlier time, i.e.,

$$\mathbf{U}_a(t) = \mathbf{U}_b(t - \Delta t). \tag{19}$$

In other words,

$$\mathbf{U}(r,\psi,z,t) = \mathbf{U}\left(r,\psi + \frac{2\pi}{N_\mathrm{B}}, z, t - \frac{T}{N_\mathrm{B}}\right), \tag{20}$$

where N_B is the number of rotor blades and $\Delta t = T/N_\mathrm{B}$. Note that we have now switched momentarily to cylindrical coordinates for simplicity. To apply these conditions, the solution $\mathbf{U}^*$ is transformed along the periodic boundaries using Eq. (12) to find the vector of Fourier coefficients $\tilde{\mathbf{U}}$ (which contains the cosine and sine

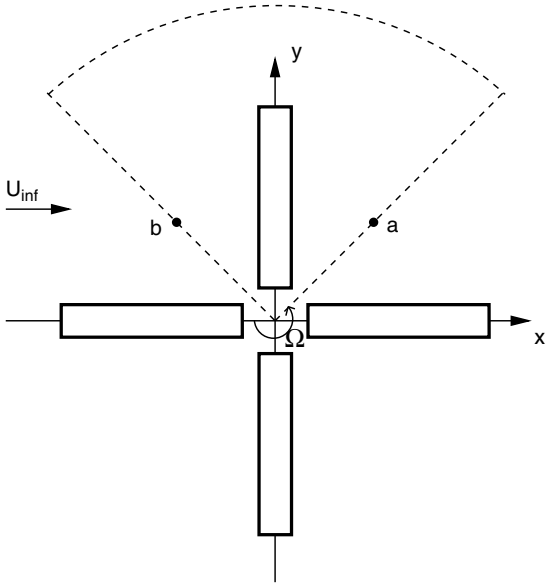

Fig. 2. Rotor periodicity condition.

coefficients $\mathbf{A}_n$ and $\mathbf{B}_n$). Inspection of Eq. (9) reveals that the appropriate boundary condition in frequency-domain is given by

$$\mathbf{A}_0\left(r,\psi+\frac{2\pi}{N_\mathrm{B}},z\right)=\mathbf{A}_0(r,\psi,z), \tag{21}$$

$$\mathbf{A}_n\left(r,\psi+\frac{2\pi}{N_\mathrm{B}},z\right)=\mathbf{A}_n(r,\psi,z)\cos\left(\frac{2\pi n}{N_\mathrm{B}}\right)+\mathbf{B}_n(r,\psi,z)\sin\left(\frac{2\pi n}{N_\mathrm{B}}\right), \tag{22}$$

$$\mathbf{B}_n\left(r,\psi+\frac{2\pi}{N_\mathrm{B}},z\right)=-\mathbf{A}_n(r,\psi,z)\sin\left(\frac{2\pi n}{N_\mathrm{B}}\right)+\mathbf{B}_n(r,\psi,z)\cos\left(\frac{2\pi n}{N_\mathrm{B}}\right), \tag{23}$$

where $n \geqslant 1$. These periodic boundary conditions allow us to reduce the computational domain to a grid spanning a single blade sector and hence reduces both the storage requirements and the computation time by a factor of N_B, the number of rotor blades.

5. Numerical results

5.1. Steady computations for ONERA M6 wing

In this section, we investigate the aerodynamics of the well-known and often analyzed ONERA M6 wing to validate our steady-flow solver. There are a number aerodynamic complexities involved with this wing, for example, the formation of a lambda shock on the upper surface, and local supersonic flow. Because of these complexities, it has been used by many researchers for code validation. The transonic ONERA M6 wing is a swept semi-span wing with no twist, and a symmetric airfoil section. The experimental data [32] for this wing were recorded for a number of transonic Mach numbers at different angles of attack. Here, we perform computations for a Mach number of 0.8395 and an angle-of-attack of 3.06. The C–H type computational grid used ($193 \times 33 \times 33$) for this case is shown in Fig. 3.

Shown in Fig. 4 is the computed surface pressure coefficient, C_p, distribution for the ONERA M6 wing at several spanwise locations. Also shown in the same figure are the experimental data and the computations obtained from the NASA-WIND [33] Navier–Stokes code. As can be seen, the overall agreement among the present computations (Duke ROTOR), NASA-WIND computations as well as the experimental data is

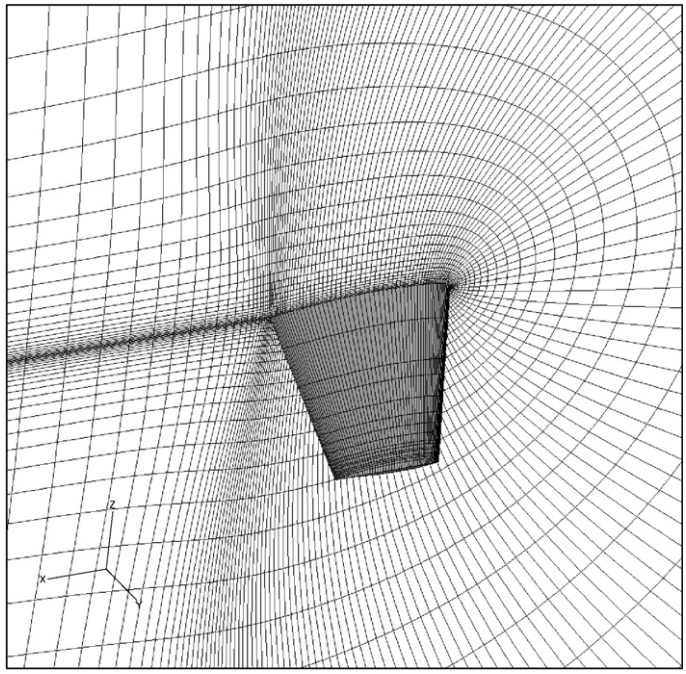

Fig. 3. ONERA M6 grid.

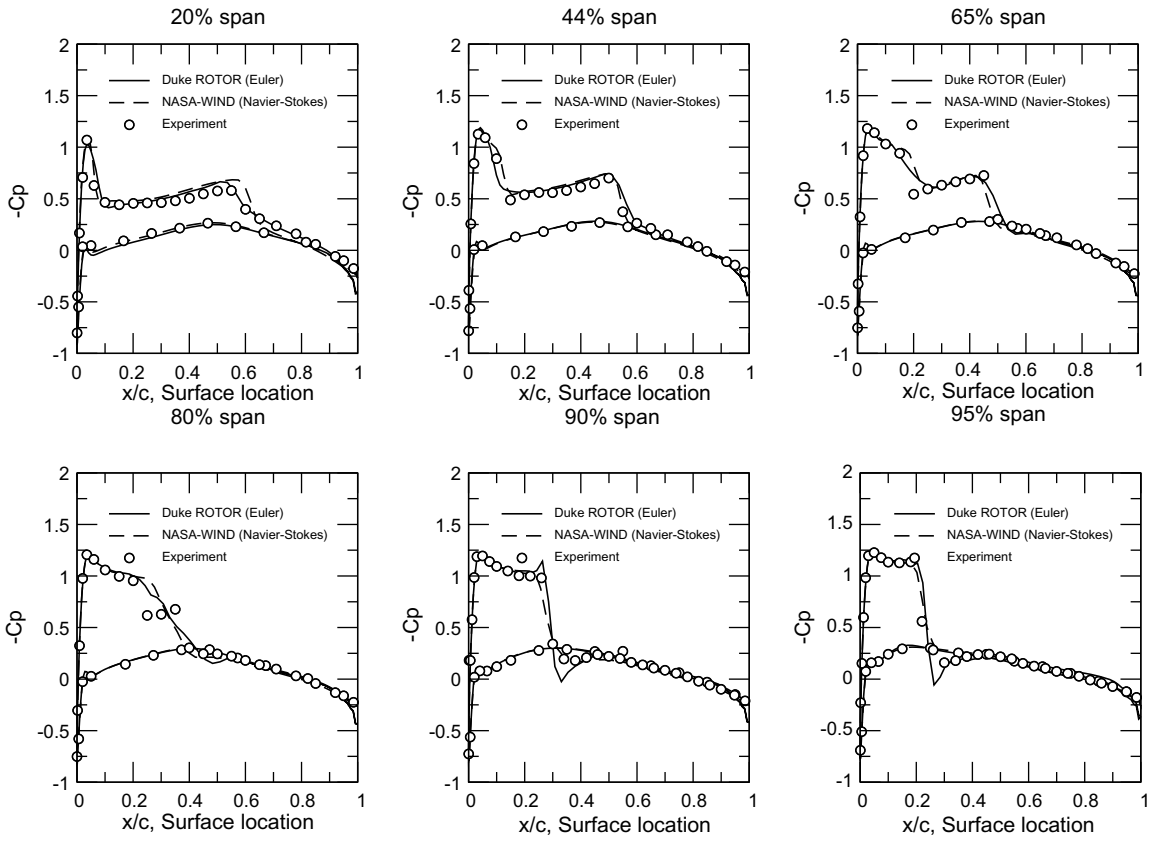

Fig. 4. Comparison of the current CFD code with NASA-WIND code and experimental data. ONERA M6 Wing.

very good. This shows that, for this case, our Euler solver can accurately predict the steady flow (shock location and pressure distribution). Fig. 5 shows the computed surface and symmetry plane pressure contours for this case. One can see that, our solver can clearly capture the "lambda-shock" forming on the suction side of the wing. Note that the same phenomenon was observed by many other researchers.

5.2. Caradonna–Tung rotor in hover

Having validated our flow solver for steady flow around a three-dimensional wing, we now move our attention to flows about rotors. In this section, we present computational results for the well-known rotor of Caradonna and Tung [34] (C–T) in hover. The C–T rotor has two untapered rectangular blades with an aspect ratio of 6 and the sections have NACA 0012 profiles. In their experiments, Caradonna and Tung [34] measured the surface pressure data at five different spanwise locations for a number of collective pitch angles and rotational speeds. The case considered in this paper has a tip Mach number, M_{tip} of 0.877 and a collective pitch angle of 8.0°. Here, we use a grid that has $193 \times 33 \times 33$ nodes (with 17 nodes on the blade in spanwise direction). The outer boundary as well as the top and bottom boundaries were placed at a distance of two blade spans above and below the rotor. Figs. 6 and 7 show the grid used for the computations in this case. Note that because periodic boundary conditions are used in this work, one only needs to generate a grid spanning a single blade sector.

We first investigate the static pressure contours around the rotor blade for six different span locations. As can be seen from Fig. 8 the flow is subsonic out to 80% span of the outboard of this location and the flow is transonic with a strong shock towards the tip of the blade. This feature is expected since the tip speed of the rotor is transonic for the case considered here. Next, we plot the surface pressure coefficient at five span locations where the experimental data is available. Shown in Fig. 9 are the computed C_p distributions as well as the experimental values [34]. One can see that the agreement with the experiment is very good except on the suction surface at 68% span. Our computations predict lower values of C_p for this section. We note that similar results were obtained by other researchers (for example, see Srinivasan and McCroskey [5]) for the 68% section. In this study, we do not use the sink boundary conditions for hover suggested by Srinivasan et al. [9], which may be the cause of this discrepancy.

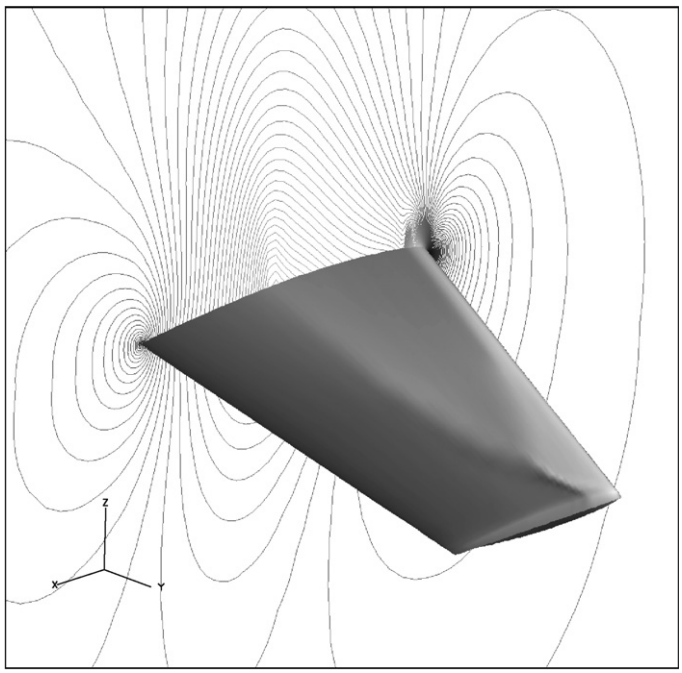

Fig. 5. Computed pressure contours on the ONERA M6 wing surface and the symmetry plane.

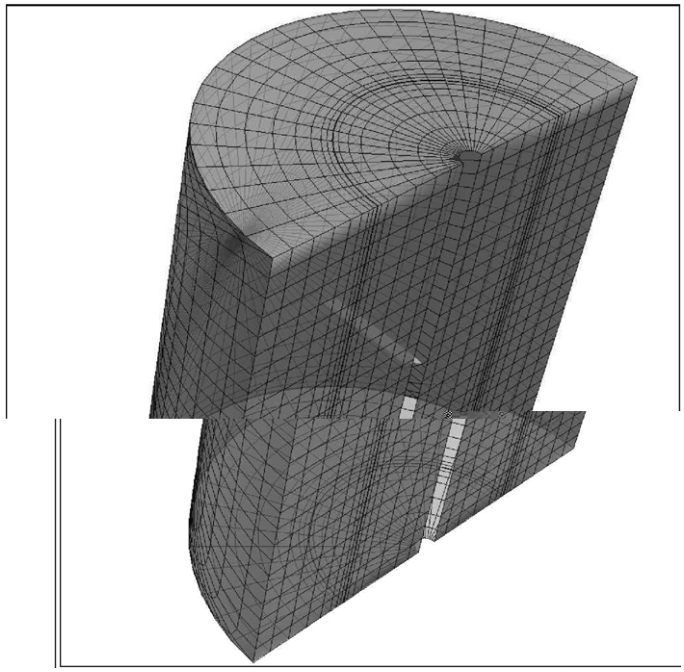

Fig. 6. Three-dimensional O–H computational grid used for C–T rotor in hover.

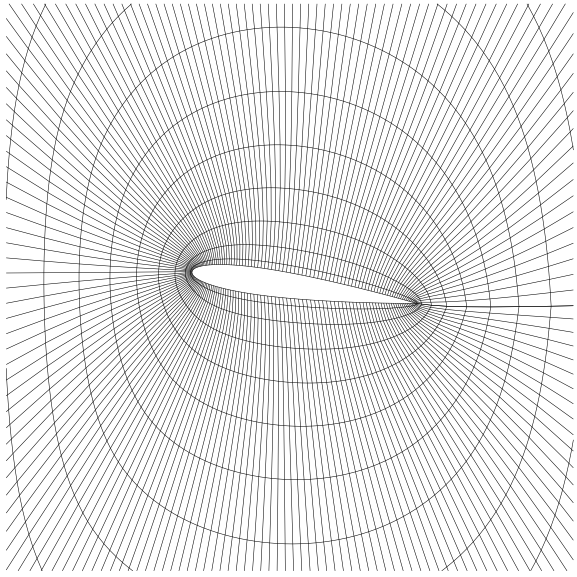

Fig. 7. Representative two-dimensional O-grid around the rotor blade.

5.3. Caradonna–Tung rotor in non-lifting forward flight

In this section, we present numerical results for unsteady flow about the C–T rotor in non-lifting forward flight. The rotor used here is comprised of two rectangular planform blades with no twist, no collective pitch and an aspect ratio of 7. A number of investigators [11,12] have used this case for validating their numerical tools, comparing their results to the available experimental data [35]. As in the previous hover case, we used a

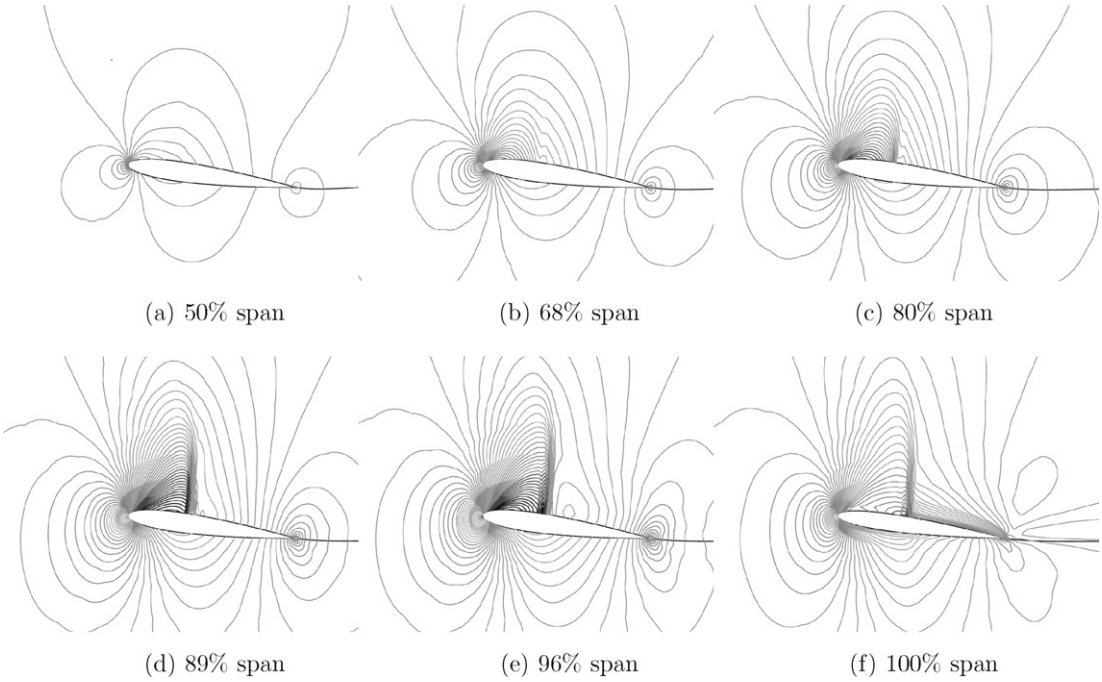

Fig. 8. Computed static pressure contours for C–T rotor in hover. (a) 50% span; (b) 68% span; (c) 80% span; (d) 89% span; (e) 96% span; (f) 100% span.

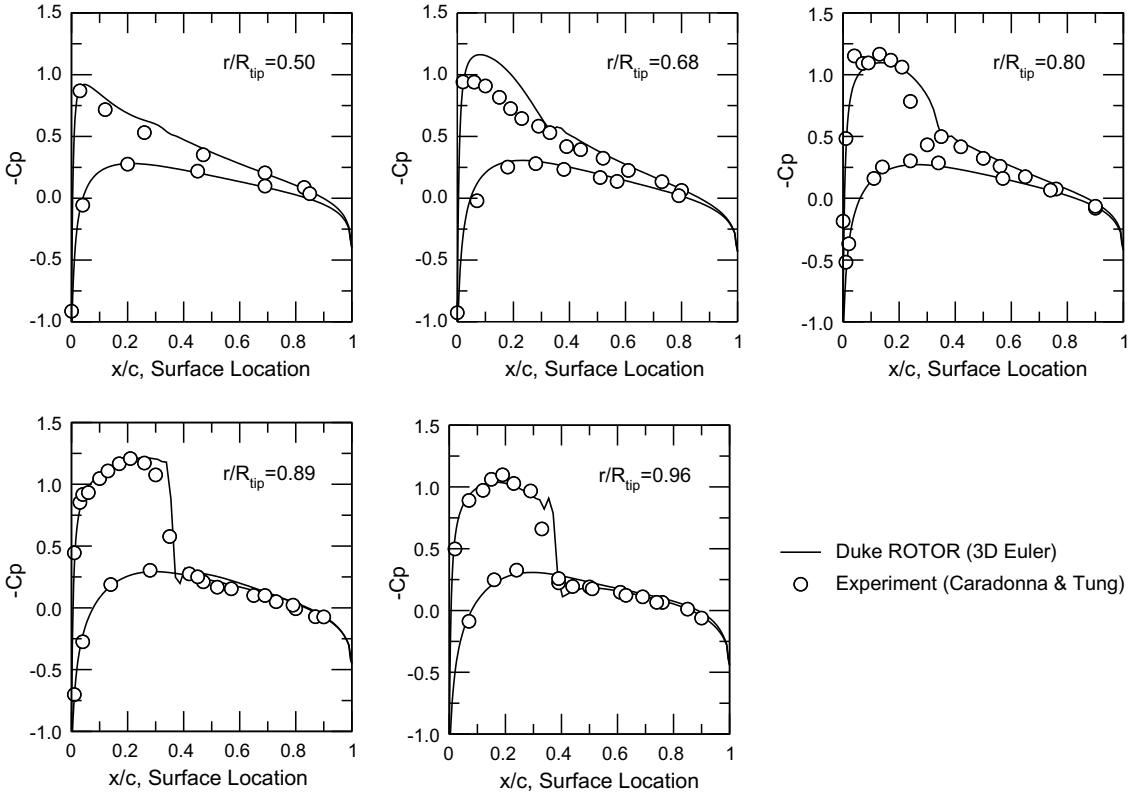

Fig. 9. C_p distribution on blade surface for C–T rotor in hover.

grid with $193 \times 33 \times 33$ grid points. The flow has strong transonic effects on the advancing blade because of the high tip Mach number ($M_{tip} = 0.8$) and moderately high advance ratio ($\mu = 0.2$).

For the following unsteady computations, we retained a total of nine harmonics (19 sub-time level solutions). These solutions were all marched to convergence making use of the HDHB equations and the pseudo-spectral operator to obtain the unsteady flow in forward flight. Fig. 10 shows the contour plots of the static pressure on the suction surface of the blade at these 19 sub-time levels, corresponding to 19 azimuth angles. It can be seen that a time-dependent shock forms on the advancing side and disappears on the retreating side. These results are in good agreement with the time-accurate computations of Pomin and Wagner [11].

As mentioned previously, the computations are performed on a grid spanning only a single blade sector and the flow may be reconstituted for other sectors using the complex periodic boundary conditions. As an example, Fig. 11 shows the density contours plotted in the plane of the rotor. Note that we only computed the flow for the advancing half of the domain. The flow in the retreating half is reconstituted using the periodic boundary conditions. It can clearly be seen that the flow in the two sectors is different because of the asymmetry caused by forward flight. It can also be seen that the contour lines at the periodic boundaries are smooth and continuous.

Next we compare our results (nine harmonics) to the experimental data of Caradonna et al. [35] shown in Fig. 12 is the C_p distribution at the 89% span of the blade at different azimuth angles, ψ. As can be seen, the agreement between our computations and the experiments is very good. The location as well as the strength of the shock is accurately predicted demonstrating once again the accuracy of our method.

The previous unsteady flow results presented in this section were obtained for nine harmonics using the HDHB method. We now turn our attention to the number of harmonics retained in the model and investigate its effect on the accuracy of the computation. For this study, we compute the unsteady flow using 1, 5, 9, and 13 harmonics. In rotorcraft aerodynamics, the lower harmonics usually are more important than the higher ones because they contribute the most to the noise generated by the rotor. Therefore, we compute the zeroth harmonic (mean) and the first harmonic of the surface pressure at 89% span location. As shown in Fig. 13, the solutions computed using 5, 9, and 13 harmonics are in good agreement for the mean quantities, whereas the solution computed using one harmonic misses some of the details of the flow. For example, the shock location

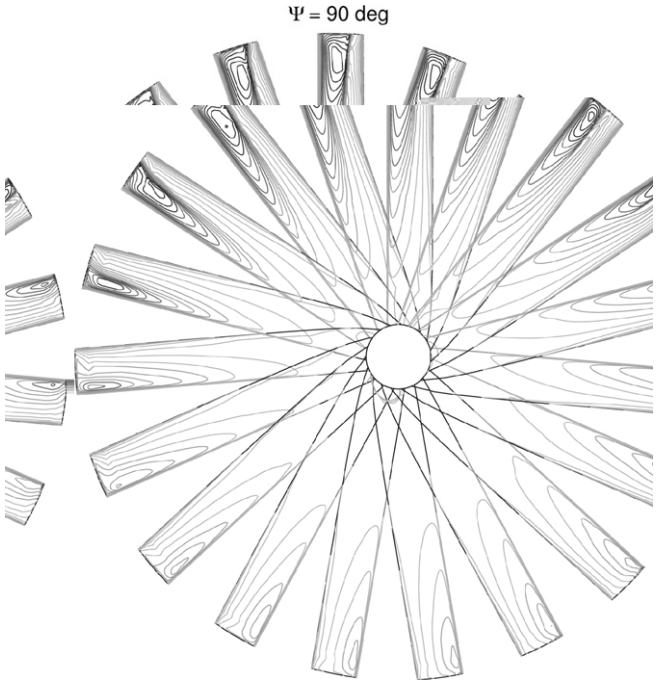

Fig. 10. Surface pressure contours at different azimuth angles (nine harmonics retained in the analysis).

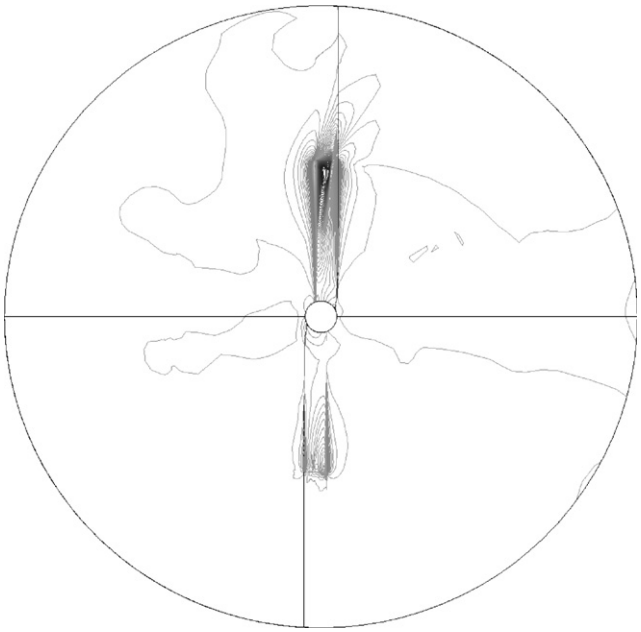

Fig. 11. Density contours in the plane of rotor. Complex periodic boundary conditions allow us to use a grid with only one blade sector.

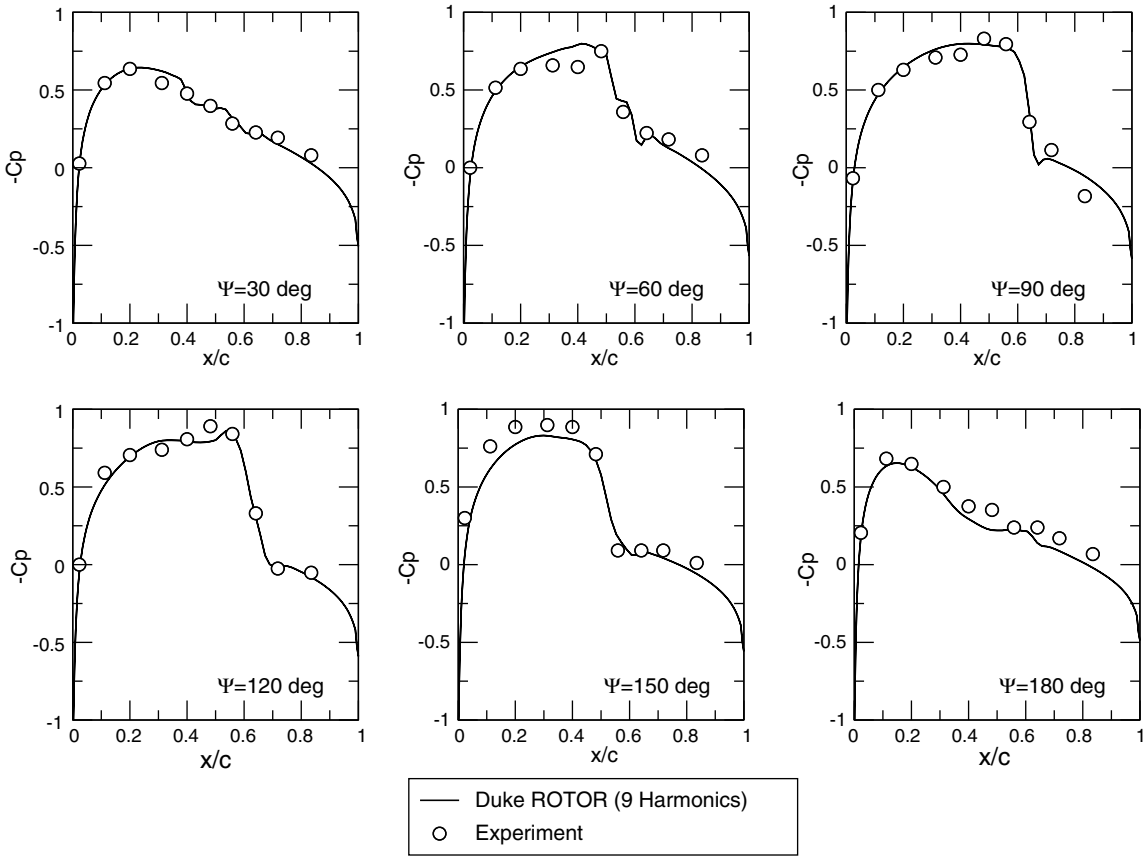

Fig. 12. Surface C_p distribution at 89% span.

is predicted to be slightly farther downstream for one harmonic. It can also be seen from the real and imaginary parts of the first harmonic of the unsteady pressure that the solutions computed using 9 and 13 harmonics are in good agreement with one another. For five harmonics, however, some of the details cannot be accurately captured. Nevertheless, the overall agreement among five and higher harmonic solutions are within engineering accuracy. This implies that for this problem, one can use as few as five harmonics (11 sub-time level solutions) to accurately model the unsteady flow.

Finally, for this same case, we present the convergence histories for different number of harmonics retained in the analysis. Fig. 14 shows that for no multigrid acceleration, the computations for the steady solution (hover), and unsteady solutions using 1, 5, 9, and 13 harmonics converge in about 4000 iterations. Also shown in the same figure is the convergence history for five harmonics with two levels of multigrid acceleration. With two levels of multigrid acceleration, the solution converges in about 1000 iterations. Table 1 shows the computational for a single iteration. Note that for all cases the computational times are normalized with respect to the steady-state computational time. As can be seen, for small number of sub-time levels retained in the model, i.e., $N \leqslant 11$, the cost of the unsteady computations scale linearly, and is $2N+1$ times the cost of the steady solution. However, as the number of sub-time levels is increased, the cost of the unsteady solutions is not exactly linear due to the increased cost of the time derivative computation. The same behavior was also

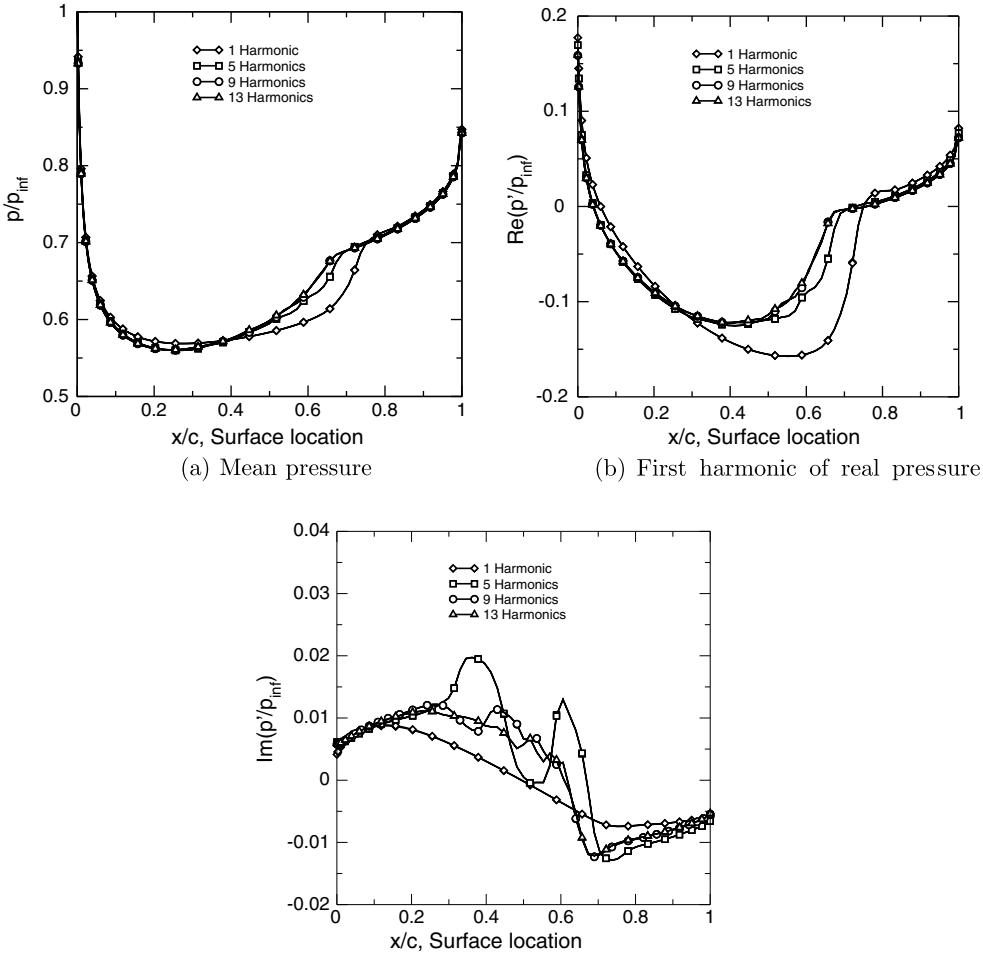

(a) Mean pressure

(b) First harmonic of real pressure

(c) First harmonic of imaginary pressure

Fig. 13. Effect of number of harmonics retained in the analysis.

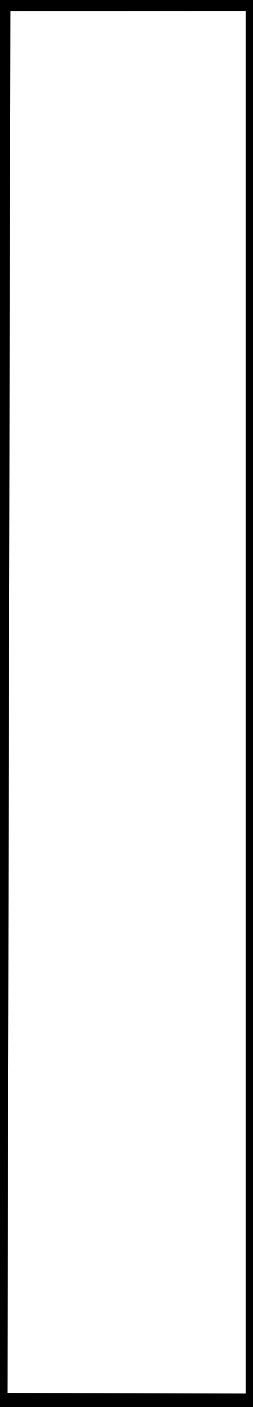

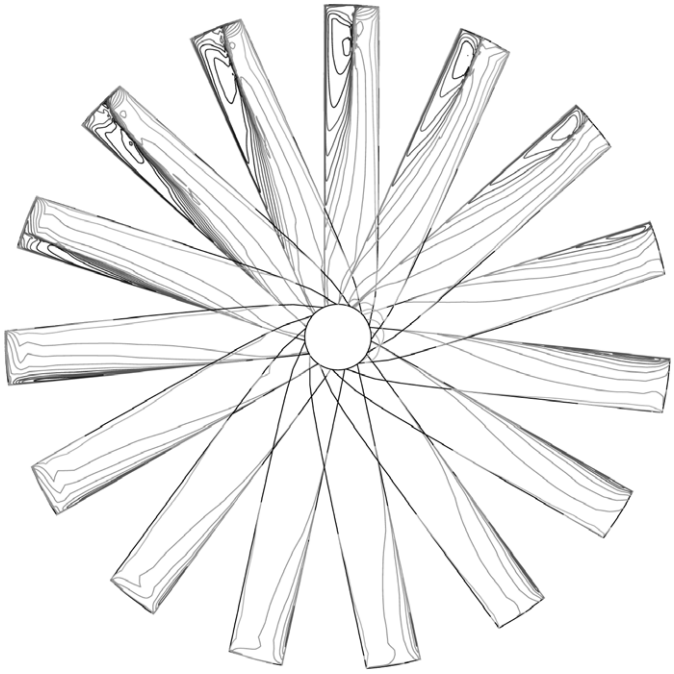

Fig. 15. Surface pressure contours for lifting C–T rotor at different azimuth angles (seven harmonics used in the analysis).

where F_z is the force on the blade in the z direction. After computing the values of C_L in time domain, one can easily use the discrete Fourier transformation matrix, **E**, and obtain the Fourier coefficients of C_L. Table 2 shows the zeroth, first and the second harmonics of C_L. As can be seen, the solution is nearly converged when one uses seven harmonics to model the unsteady flow. The same can also be seen from the pressure contour plots at 90° azimuth angle and 89% span, where the transonic nonlinear effects are strongest, as shown in Fig. 16. Note that seven and eleven harmonic solutions are in good agreement with one another but differ somewhat from the solution computed using three harmonics. Next, we compare the values of C_L computed using 1, 3, 5, 7, 9, and 11 harmonics at different azimuth angles. Fig. 17 clearly shows the effect of number of harmonics used. We observe that the solution computed using five harmonics is nearly converged. This once again implies that one only needs a handful harmonics to accurately compute strongly nonlinear flows in forward-flight.

Finally, we plot the values of C_L at different azimuth angles and compare our results to those of Allen. As seen in Fig. 18, the agreement between the two solvers is excellent. Our computations seem to have a slightly weaker blade-vortex interaction compared to Allen's computations, but otherwise agree quite well.

Table 2
Harmonics of rotor load coefficient for non-lifting C–T rotor in forward-flight

Harmonics	C_{L_0}	C_{L_1}	C_{L_2}
1	0.2419	(0.0231, −7.1627E − 03)	
3	0.2168	(0.1017, −2.2010E − 02)	(5.9153E − 03, −3.1381E − 02)
5	0.2152	(0.1382, −3.1691E − 02)	(1.6361E − 02, −4.6781E − 02)
7	0.2148	(0.1536, −3.5636E − 02)	(1.8821E − 02, −5.2767E − 02)
9	0.2161	(0.1565, −3.6433E − 02)	(1.7086E − 02, −5.3545E − 02)
11	0.2156	(0.1569, −3.6888E − 02)	(1.5854E − 02, −5.2950E − 02)

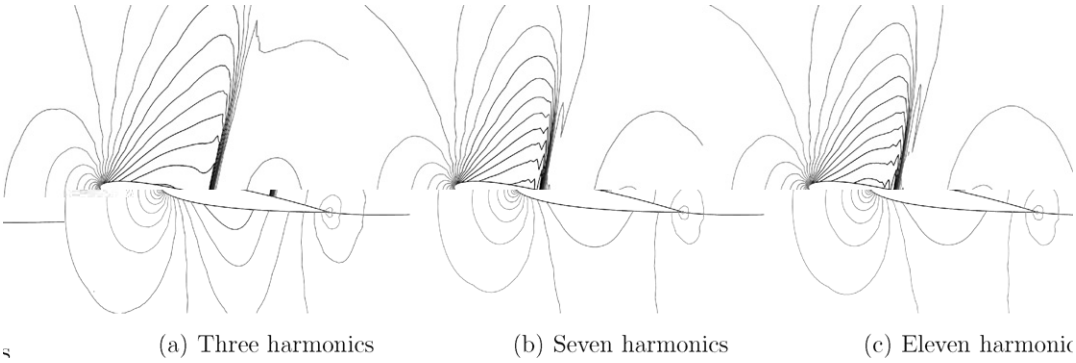

Fig. 16. Pressure contours at $\psi = 90°$ and $r/R_{tip} = 0.89$.

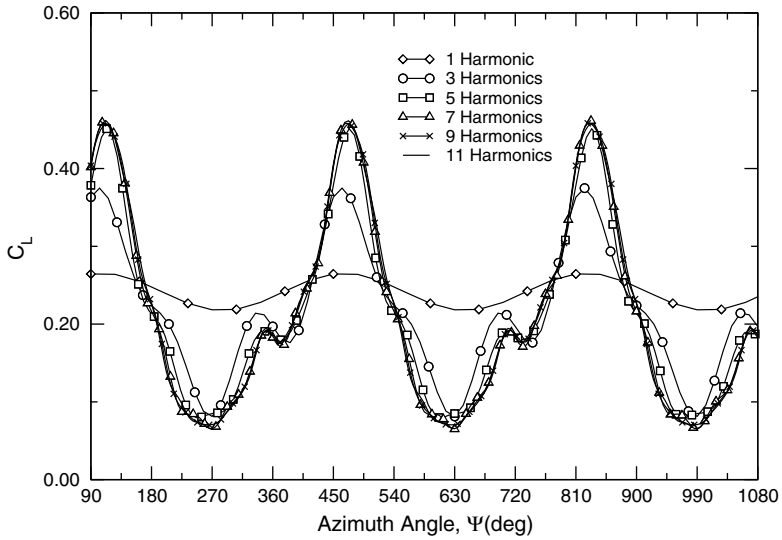

Fig. 17. The effect of number of harmonics used in the analysis.

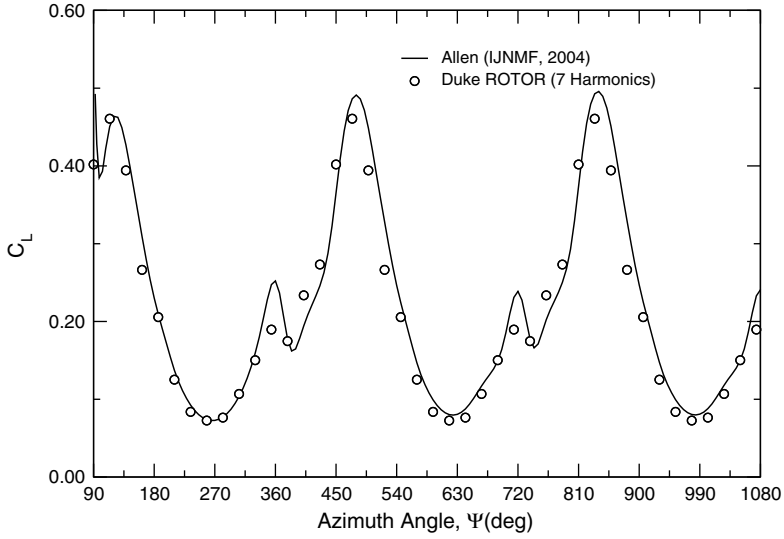

Fig. 18. Comparison of the present technique to a time-accurate solver (seven harmonics used in the analysis).

6. Conclusions

In this study, we have applied a state of the art high-dimensional harmonic balance technique to predict unsteady aerodynamics about helicopter rotors. We have demonstrated that our code can accurately model both unsteady (forward-flight) and steady (hover) flows for the test cases presented in this paper. We have also shown that strongly nonlinear flows can be modeled to engineering accuracy with a small number of harmonics. Thus, the method is computationally efficient, requiring computational times that scale with the number of sub-time levels in the model times the cost of a single steady computation. By contrast, the cost of a conventional time-marching calculation is about two orders of magnitude greater than that of a steady solution. Our method also has other distinct advantages over its time-domain equivalents. First, using complex periodicity conditions, the computational domain can be reduced to a grid spanning a single blade sector. Second, using the pseudo time marching technique, the governing equations can be solved using steady-state acceleration techniques such as local time stepping and multigrid acceleration. Finally, although the method was presented for inviscid flows, it can be generalized to viscous cases and indeed viscous flow solutions for fixed wings are already available in the literature.

Acknowledgment

This work was sponsored by a Short Term Innovative Research (STIR) project grant from the US Army Research Office (Grant No. W911NF-06-1-0370) with technical oversight provided by Dr. Tom Doligalski. We also thank Dr. C.B. Allen of Bristol University for providing numerical results from his time-accurate analysis to which we compared our results in this paper.

References

[1] R.C. Strawn, C. Tung, The prediction of transonic loading on advancing helicopter rotors, Technical Manual NASA TM-88238, NASA Ames Research Center, Moffett Field, CA, April 1986.
[2] R.C. Strawn, F.X. Caradonna, Conservative full potential model for unsteady transonic rotor flows, AIAA Journal 25 (2) (1987) 193–198.
[3] R.K. Agarwal, J.E. Deese, Euler calculations for flowfield of a helicopter rotor in hover, Journal of Aircraft 24 (4) (1987) 231–238.
[4] B.E. Wake, L.N. Sankar, Solution of the Navier–Stokes equations for the flow about a rotor blade, Journal of the American Helicopter Society 34 (2) (1989) 13–23.
[5] G.R. Srinivasan, W.J. McCroskey, Navier–Stokes calculations of hovering rotor flowfields, Journal of Aircraft 25 (10) (1988) 865–874.
[6] C.L. Chen, W.J. McCroskey, S. Obayashi, Numerical solutions of forward-flight rotor flow using an upwind method, Journal of Aircraft 28 (6) (1991) 374–380.
[7] G.R. Srinivasan, J.D. Baeder, S. Obayashi, W.J. McCroskey, Flowfield of a lifting rotor in hover: a Navier–Stokes simulation, AIAA Journal 30 (10) (1992) 2371–2378.
[8] G.R. Srinivasan, J.D. Baeder, TURNS: A free-wake Euler/Navier–Stokes numerical method for helicopter rotors, AIAA Journal 31 (5) (1993) 959–962.
[9] G.R. Srinivasan, V. Raghavan, E.P.N. Duque, W.J. McCroskey, Flowfield analysis of modern helicopter rotors in hover by Navier–Stokes method, Journal of the American Helicopter Society 38 (3) (1993) 3–10.
[10] A. Bangalore, L.N. Sankar, Forward-flight analysis of slatted rotors using Navier–Stokes methods, Journal of Aircraft 34 (1) (1997) 80–86.
[11] H. Pomin, S. Wagner, Navier–Stokes analysis of helicopter rotor aerodynamics in hover and forward flight, Journal of Aircraft 39 (5) (2002) 813–821.
[12] C.B. Allen, An unsteady multiblock multigrid scheme for lifting forward flight rotor simulation, International Journal for Numerical Methods in Fluids 45 (9) (2004) 973–984.
[13] R. Steijl, G. Barakos, K. Badcock, A framework for CFD analysis of helicopter rotors in hover and forward flight, International Journal for Numerical Methods in Fluids 51 (8) (2006) 819–847.
[14] C.B. Allen, Parallel universal approach to mesh motion and application to rotors in forward flight, International Journal for Numerical Methods in Engineering 69 (10) (2007) 2126–2149.
[15] A.T. Conlisk, Modern helicopter rotor aerodynamics, Progress in Aerospace Sciences 37 (5) (2001) 419–476.
[16] R.C. Strawn, F.X. Caradonna, E.P.N. Duque, 30 years of rotorcraft computational fluid dynamics research and development, Journal of the American Helicopter Society 51 (1) (2006) 5–21.

[17] K.C. Hall, Computation of unsteady nonlinear flows in cascades using a harmonic balance technique, Presented at the Kerrebrock Symposium, A Symposium in Honor of Professor Jack L. Kerrebrock's 70th Birthday, The Massachusetts Institute of Technology, Cambridge, Massachusetts, January 1998.
[18] K.C. Hall, J.P. Thomas, W.S. Clark, Computation of unsteady nonlinear flows in cascades using a harmonic balance technique, Presented at the 9th International Symposium on Unsteady Aerodynamics, Aeroacoustics and Aeroelasticity of Turbomachines, Lyon, France, September 2000.
[19] K.C. Hall, J.P. Thomas, W.S. Clark, Computation of unsteady nonlinear flows in cascades using a harmonic balance technique, AIAA Journal 40 (5) (2002) 879–886.
[20] R.L. Davis, T. Shang, J. Buteau, R.H. Ni, Prediction of 3-d unsteady flow in multi-stage turbomachinery using an implicit dual time-step approach, AIAA Paper 96-2565, 1996.
[21] M. McMullen, A. Jameson, J.J. Alonso, Application of a non-linear frequency domain solver to the Euler and Navier-Stokes equations, AIAA Paper 2002-120, 2002.
[22] M. McMullen, A. Jameson, J.J. Alonso, Demonstration of non-linear frequency methods, AIAA Journal 44 (7) (2006) 1428–1435.
[23] K. Ekici, K.C. Hall, Nonlinear analysis of unsteady flows in multistage turbomachines using harmonic balance, AIAA Journal 45 (5) (2007) 1047–1057.
[24] A. Gopinath, E. van der Weide, J.J. Alonso, A. Jameson, K. Ekici, K.C. Hall, Three-dimensional unsteady multi-stage turbomachinery simulations using the harmonic balance technique, AIAA Paper 2007-0892, 2007.
[25] J.P. Thomas, K.C. Hall, E.H. Dowell, C. Denegri, Modeling limit cycle oscillation behavior of the F-16 fighter using a harmonic balance approach, AIAA Paper 2004-1696, 2004.
[26] G.E. Welch, Application of harmonic balance technique to the compressible Euler and Navier-Stokes equations, AIAA Paper 2007-844, 2007.
[27] S. Choi, J.J. Alonso, E. van der Weide, J. Sitaraman, Validation study of aerodynamic analysis tools for design optimization of helicopter rotors, AIAA Paper 2007-3929, June 2007.
[28] M. Kumar, V.R. Murthy, Analysis of flow around multibladed rotor using CFD in the frequency domain, AIAA Paper 2007-3806, June 2007.
[29] R.H. Ni, A multiple-grid scheme for solving the Euler equations, AIAA Journal 20 (11) (1982) 1565–1571.
[30] A.I. Sayma, M. Vahdati, L. Sbardella, M. Imregun, Modeling of three-dimensional viscous compressible turbomachinery flows using unstructured hybrid grids, AIAA Journal 38 (6) (2000) 945–954.
[31] J.L. Thomas, M.D. Salas, Far-field boundary conditions for transonic lifting solutions to the Euler equations, AIAA Journal 24 (7) (1986) 1074–1080.
[32] V. Schmitt, F. Charpin, Pressure distributions on the ONERA-M6-Wing at transonic Mach numbers, Experimental Data Base for Computer Program Assessment, Report of the Fluid Dynamics Panel Working Group 04, AGARD (AR-138).
[33] K.E. Tatum, J.W. Slater, The validation archive of the NPARC alliance, AIAA Paper 99-0747, 1999.
[34] F.X. Caradonna, C. Tung, Experimental and analytical studies of a model helicopter rotor in hover, Technical Manual NASA TM–81232, NASA Ames Research Center, Moffett Field, CA, September 1981.
[35] F.X. Caradonna, G.H. Laub, C. Tung, An experimental investigation of the parallel blade–vortex interaction, Technical Manual NASA TM–86005, NASA Ames Research Center, Moffett Field, CA, November 1984.